Materials Advances

ROYAL SOCIETY OF CHEMISTRY

PAPER

View Article Online
View Journal

Cite this: DOI: 10.1039/d5ma00896d

Short-time spreading dynamics of elastic drops

Surjyasish Mitra,[a] A-Reum Kim,[b] Boxin Zhao[b] and Sushanta K. Mitra*[a]

Received 13th August 2025,
Accepted 16th December 2025

DOI: 10.1039/d5ma00896d

rsc.li/materials-advances

When a liquid drop makes first contact with any surface, the unbalanced surface tension force drives the contact line, causing spreading. For Newtonian or weakly elastic, non-Newtonian liquids, either liquid inertia or viscosity, or a combination of the two, resists spreading. In this work, we investigate how drop elasticity influences spreading dynamics. We conduct dynamical experiments with polyacrylamide drops of varying polymer concentrations to impart varying degrees of elasticity. Using high-speed imaging, we focus on the very first moments of spreading on glass substrates. For moderate and high Young's modulus values, we observe that the early-time spreading dynamics obey a viscous-capillary regime characterized by a power-law evolution of the spreading radius. However, the process transitions to a different regime on a timescale comparable to the characteristic viscoelastic relaxation timescale. We interpret this latter regime using a theoretical model invoking the standard linear model of viscoelasticity. For viscoelastic inks with moderate print speeds, the dynamical behavior investigated in this study can provide valuable insights into how to efficiently control such moving contact lines with non-trivial elasticity.

1 Introduction

When a liquid drop is gently deposited on any rigid substrate, it spreads spontaneously until equilibrium is reached.[1,2] On the same substrate, a rigid sphere sits as deposited with a finite, small contact radius.[3,4] These two extreme scenarios *vis-a-vis* wetting and contact adhesion have been treated independently using classical theories of Young[5] and Hertz[3]/Johnson–Kendall–Roberts (JKR),[4] respectively. However, between these two configurations lies a plethora of intermediate contact/wetting morphologies, primarily modulated by the substrate wettability and elasticity (Fig. 1). The effect of surface wettability is more pronounced for wetting than for contact adhesion, whereas modulating the surface's elastic modulus causes profound changes in both cases. For instance, making the substrate sufficiently soft enables a configuration where a sessile liquid drop exhibits deformation at the three-phase contact line, generating a wetting ridge structure.[6–9] Similarly, increased indentation depths can be observed for contacts of rigid spheres on soft substrates.[10] Despite such insights, many unanswered questions still remain. Primarily among them is the effect of the elasticity of the top pair. In recent studies using elastic hydrogel spheres, it was shown that configurations intermediate between wetting and contact emerge upon modulating the elastic modulus of the hydrogels.[11,12] Typically, hydrogels consist of a solid network of crosslinked natural or synthetic polymers swollen with water.[13,14] The primary polymer network imparts the desired elastic modulus of the hydrogel.[13] By tuning the relative concentration of this primary polymer network in our earlier work, we prepared polyacrylamide hydrogels with Young's modulus varying from a few millipascals to hundreds of kilopascals and demonstrated how one can translate from a wetting-like morphology to a contact-like morphology upon contact with any substrate.[11] Essentially, for weakly elastic hydrogels, a Newtonian-liquid-drop-like wetting morphology was observed, whereas for highly elastic hydrogels, a non-wetting, rigid-sphere-like contact morphology was observed.[11] Furthermore, to interpret this transition from wetting to contact with increasing elasticity, we employed density functional theory.[15] Consequently, it was shown that a switch from attractive to repulsive interaction potential between an elastic wedge and a rigid substrate enables this transition from wetting to contact with increasing Young's modulus.[15] However, for any contacting system to reach equilibrium, it has to go through a finite transient stage. Typically, this transient dynamics on rigid and soft substrates[16–19] is well studied for the wetting of liquids, *i.e.*, spreading.

For spreading of Newtonian liquid drops with well-defined liquid properties such as density, surface tension, and viscosity, the dynamics can be well defined using phenomenological scaling laws that account for the dominant driving and resistive

[a] *Department of Mechanical & Mechatronics Engineering, Waterloo Institute for Nanotechnology, University of Waterloo, Waterloo, Ontario N2L 3G1, Canada. E-mail: skmitra@uwaterloo.ca*
[b] *Department of Chemical Engineering, Waterloo Institute for Nanotechnology, University of Waterloo, Waterloo, Ontario N2L 3G1, Canada. E-mail: zhaob@uwaterloo.ca*

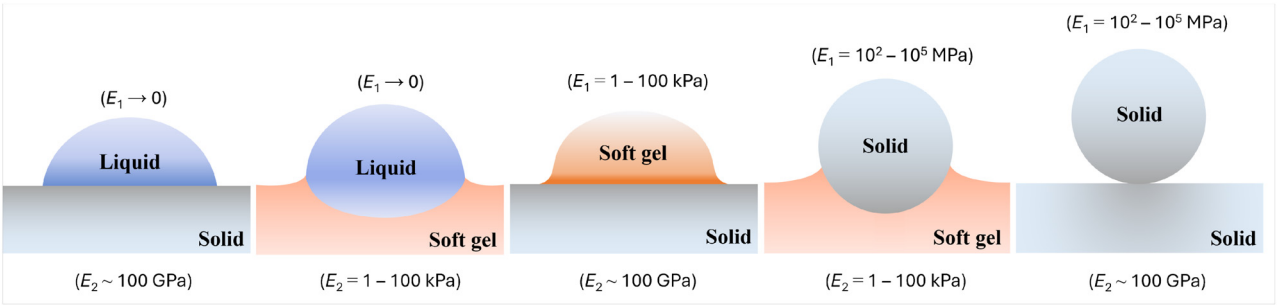

Fig. 1 Schematic showing the different possible contact/wetting morphologies upon varying the elasticity of the top (Young's modulus, E_1) and bottom (Young's modulus, E_2) pair. Representative E_1 and E_2 values are shown.

forces.[16–18,20] It is well understood that liquid surface tension drives the spreading process, whereas liquid inertia[16,17,21] or viscosity[18,20,22] opposes it. Consequently, we observe scaling laws representing the evolution of the drop-substrate footprint radius r as $r \sim t^{\alpha}$, where the power-law exponent α typically assumes values of 1 (inertia-limited viscous,[18,23,24] early), 0.5 (inertia,[16,17,21] early), and 0.1 (contact line dissipation,[25,26] late) depending on the dominant resistive force and the relevant stage of spreading. Furthermore, modulating the substrate properties, such as making the substrate hydrophobic, causes variation in the power-law exponent.[17] In certain cases, deviations from power-law spreading are also observed. For instance, making the underlying substrate sufficiently soft causes the spreading radius to transition from the early-time inertial scaling law and follow a trajectory that can be best described using an exponential relaxation function.[27] However, despite such extensive studies on the spreading dynamics with varying liquid and substrate properties, outstanding questions still remain. As mentioned previously, primarily among them is what happens when we impart elasticity to the drop phase. This dynamic elastowetting phenomenon is widely relevant for cell spreading, where cells are often modeled as elastic membrane-bound shells, whose early-time spreading behavior obeys power-law scaling.[28]

It is worth noting that existing literature mostly reports the spreading of viscoelastic liquids.[29,30] These are either weakly elastic polymeric solutions, such as polyethylene oxide (PEO) and FLOPAM, or low concentrations of polyacrylamide (PAAm) and polyvinyl alcohol (PVA) solutions.[29–31] For such cases, the shear storage modulus G' is typically smaller than the shear loss modulus G'',[31,32] and hence the materials behave more like viscous liquids rather than viscoelastic materials or even elastic solids. They are typically characterized using their zero-shear-rate or high-shear-rate viscosity obtained from shear-rate ramp measurements.[29,30] For instance, Bouillant *et al.*[29] and Yada *et al.*[30] conducted spreading experiments with low concentrations of PEO solutions where the zero-shear-rate viscosity varied between 10 mPa s and 10 Pa s. Consequently, their early-time spreading behavior was found to mirror that of Newtonian liquids such as water. As a result, their spreading characteristics were described similarly using liquid inertia or rate-dependent viscosity (zero shear or high shear) since their elastic (or shear) modulus, often on the order of a few pascals, is not dominant. Consequently, the role of a non-trivial, finite elastic modulus in this transient dynamics remains elusive. In this work, we probe the spreading of elastic drops/spheres with Young's modulus varying between 0.1 kPa and 400 kPa on glass substrates.

The choice of the Young's modulus range is driven by the following factors. First, our previous work on the static morphologies of elastic drops/spheres indicated that such materials exhibit significant morphological changes in the aforementioned Young's modulus range.[11] When the material's Young's modulus is on the order of tens of pascals or lower, they exhibit complete wetting configurations on substrates like glass, similar to a Newtonian liquid like DI water or weakly elastic polymeric liquids such as PEO.[33] Furthermore, with increasing Young's modulus, the elastic drops bead up like glass spheres and beyond 500 kPa, they exhibit no discernible contact radius change.[11] Second, for optimal print efficiency in many 3D printing applications using biomaterial inks, it is desired that the material is neither too elastic nor too viscous.[34] Hence, our choice of PAAm Young's modulus perfectly fits that requirement.

2 Materials and methods

2.1 Fabrication of elastic drops

To enable broad control of Young's modulus E, we prepared 1 mm radius polyacrylamide (PAAm) drops/spheres, which behave as polymeric liquid drops at low polymer concentrations, exhibit intermediate morphologies at moderate concentrations, and behave as elastic spheres mimicking rigid beads at high concentrations.[11] Briefly, the elastic drops were produced using an in-house recipe consisting of acrylamide (monomer), *N*,*N*′-methylene-bis-acrylamide (BIS) (crosslinker), and 2,4,6-tri-methyl benzoyldiphenylphosphine oxide (TPO) (initiator) (Fig. 2). The Young's modulus of the polyacrylamide drops was varied between 0.16 kPa and 366 kPa by varying the monomer weight percentage from 6.5 to 30, whereas the necessary spherical shapes of the drops were attained by suspending them in *n*-octane and silicone oil utilizing their density gradient (Fig. 2). Further details of the fabrication

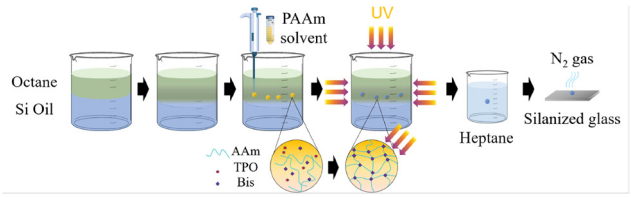

Fig. 2 Schematic showing the different steps of the preparation procedure of polyacrylamide drops/spheres. AAm: acrylamide, TPO: 2,4,6-trimethyl benzoyldiphenylphosphine oxide, and Bis: *N*,*N*′-methylene-bis-acrylamide.

process can be found in our previous works.[11,15,35] As our working substrates, we used microscope glass slides cleaned using acetone, IPA, and DI water before use.

2.2 Rheology measurements

The elastic properties of the PAAm were characterized using a rheometer. For rheology measurements, each PAAm formulation was polymerized in a Petri dish with a thickness of 2 mm. The shear storage (G') and loss (G'') moduli of the materials were measured by performing a frequency sweep test on a dynamic shear rheometer (AR 2000, TA Instruments and Kinexus Rotational Rheometer, Malvern Instruments) from 0.01 to 100 Hz at 1% strain and a normal force of 1 N. All measurements were performed at 25 °C using a 25 mm diameter plate as the test adapter. The measurements were taken after waiting 10 min for the polymer to stabilize. From the rheology measurements, it is evident that for PAAm with 6.5 wt% monomer, both G' and G'' plateau to constant values at low frequency, where $G' \gg G''$, indicating solid-like behavior (Fig. 3a). However, at high frequency, we observed that G'' becomes equal to G' and often exceeds it, indicating a transition to liquid-like behavior. However, for the stiffest PAAm, *i.e.*, with 30 wt% monomer, we observed that $G' \gg G''$ across the entire frequency range (Fig. 3b). Note that due to limitations of the rheometer, the shear modulus at higher frequencies cannot be probed. Furthermore, note that additional rheology measurements, *i.e.*, shear strain amplitude measurements, are included in the SI (see Fig. S1).

Constitutive spring–dashpot models are often used to mimic the response of viscoelastic solids and liquids, where the spring represents an elastic solid with modulus G_0 (or E_0) and the dashpot represents a Newtonian fluid with viscosity μ_0 (ref. 36) (Fig. 4a). The most common ones are the Maxwell model and the Kelvin–Voigt model (Fig. 4a). However, most real soft materials exhibit mechanical responses that can be best described using a combination of these two models.[36] The simplest combinations are called the standard linear models.[36–38] For instance, coupling a Maxwell element in parallel with another dashpot provides the well-known Oldroyd-B model, used extensively to model viscoelastic liquids[39] (Fig. 4a). Variations of the Oldroyd-B model, for

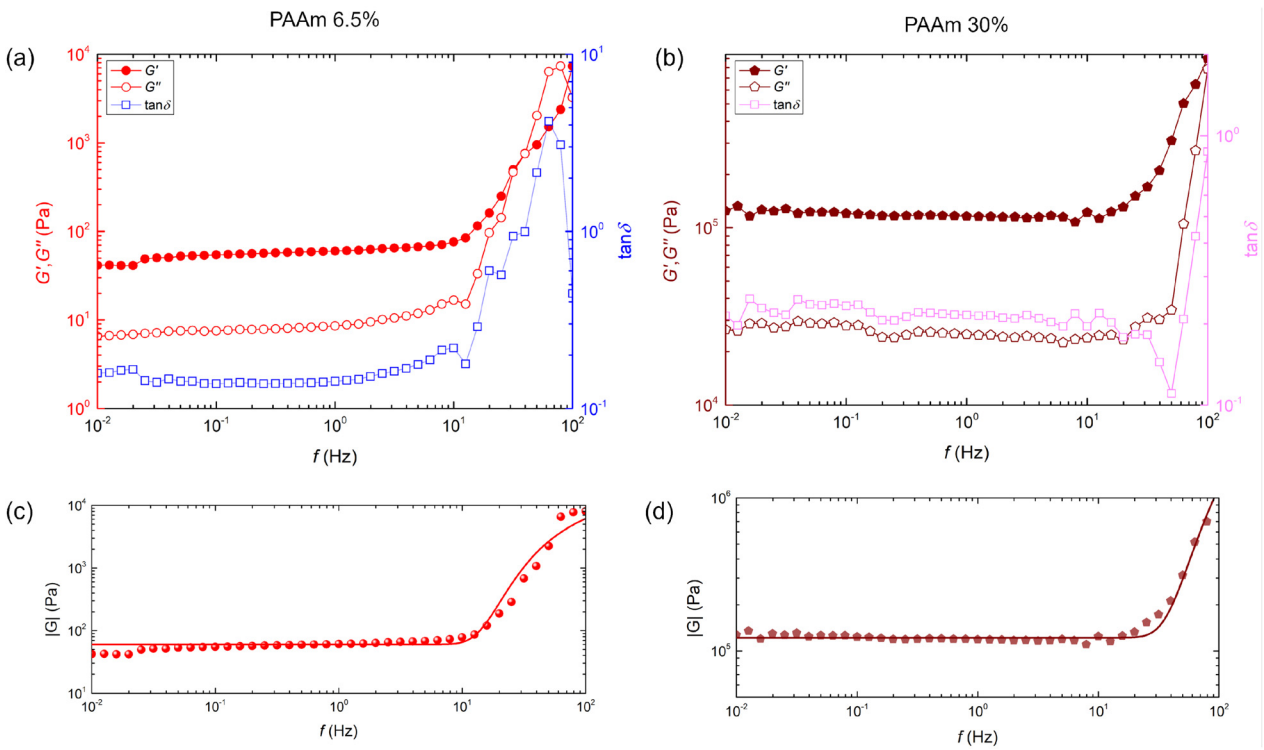

Fig. 3 Variation of shear storage modulus G', shear loss modulus G'', and loss tangent tan δ with frequency f for (a) PAAm with 6.5 wt% monomer and (b) PAAm with 30 wt% monomer. Variation of absolute shear modulus $|G| = \sqrt{G'^2 + G''^2}$ with frequency f for (c) PAAm with 6.5 wt% monomer and (d) PAAm with 30 wt% monomer. The solid lines represent the fitting equation $G_0 + (G_\infty - G_0)e^{-1/f\tau}$, where G_0 and G_∞ represent the static shear modulus and the high-frequency shear modulus, respectively. Here, τ is the relaxation time scale. Note that in fitting the rheology data, $\beta = G_\infty/G_0$ values of 200 and 20 are used for PAAm 6.5% and PAAm 30%, respectively.

instance, the Saramito model, have also been used to model the flow and dynamical behavior of viscoelastic materials.[40,41] These models inherently decouple the solvent and the polymer viscosities, μ_S and μ_P, respectively, using the two dashpots. However, for the present PAAm composition, the solvent (water) viscosity is significantly lower than the polymer viscosity, *i.e.*, $\mu_S \ll \mu_P$. Furthermore, due to the relatively higher elasticity of the materials and the dynamical nature of contact, we realized that the Oldroyd-B model is not suitable for our system. Hence, we used the standard linear model with a Kelvin–Voigt element in series with another spring. The rationale behind using this model is that it accurately maps the dynamics of the moving contact line as the elastic drops/spheres spread. Due to the finite velocity of the contact line, it is modeled using a spring with high-frequency modulus G_∞ and the dashpot represents the viscosity μ_0, whereas regions away from the contact line are modeled using a spring with relaxed modulus G_0 (Fig. 4b). Furthermore, the high-frequency spring is either unrelaxed or in the process of relaxing, depending on the magnitude of the contact line velocity (Fig. 4b).

From existing literature,[38] the relaxation function of the standard linear model can be represented as $G(t) = G_0 + (G_\infty - G_0)e^{-t/\tau}$, where τ is the relaxation timescale and t is the temporal variable. From the G' and G'' values measured from rheology, we first calculated the absolute shear modulus $|G| = \sqrt{G'^2 + G''^2}$. Consequently, we used a fitting equation of the form $G_0 + (G_\infty - G_0)e^{-1/f\tau}$ to obtain the static shear modulus G_0 and the relaxation timescale τ (see Table 1). Here, $f = 1/t$ is the frequency. The elastic modulus of the materials was consequently calculated using the relation $E_0 = 2G_0(1 + \nu) = 3G_0$, *i.e.*, considering Poisson's ratio $\nu = 1/2$ (ref. 11) (see Table 1). The viscosity of the PAAm spheres was calculated using the relation $\mu_0 = G_0\tau$. Furthermore, note that other rheology models, such as the Chasset–Thirion relation,[9,19] were found to be inappropriate for fitting the present rheology since in that model G'' decays following a power-law relation in f. In

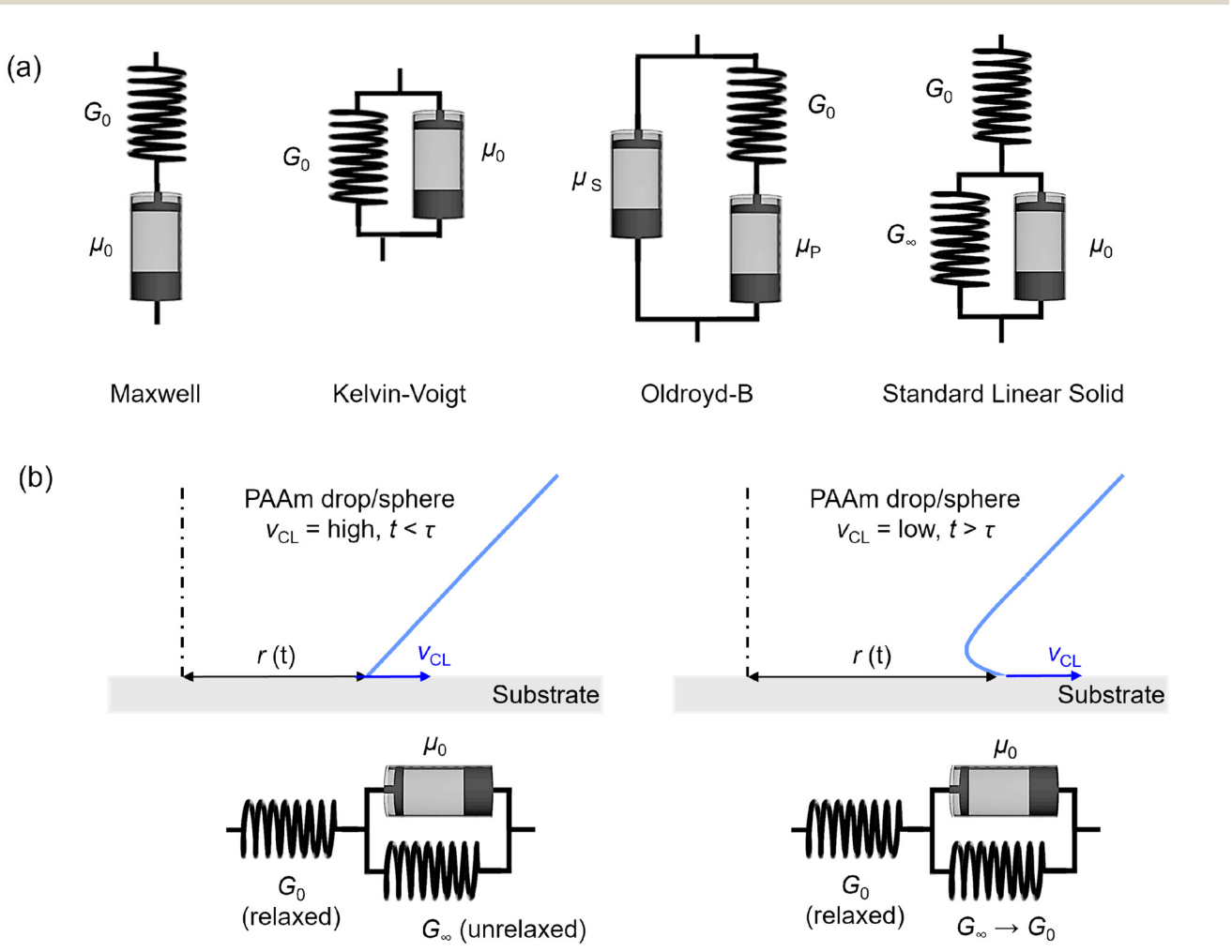

Fig. 4 (a) Spring–dashpot representation of constitutive rheology models: Maxwell, Kelvin–Voigt, Oldroyd-B, and standard linear solid. G_0 is the elastic (shear) modulus and μ_0 is the dashpot viscosity. μ_S and μ_P represent the solvent and polymer viscosities. G_∞ represents the high-frequency (or unrelaxed) modulus. (b) Schematic of the spreading process of PAAm at high and low contact-line velocities v_{CL}, and the corresponding rheology model mapping the motion. $r(t)$ and τ represent the time-dependent spreading radius and the relaxation timescale, respectively.

Table 1 Physical properties of the prepared PAAm. E_0, ρ, γ, and τ are the elastic modulus, density, surface tension, and relaxation timescale, respectively

Materials	E_0 (kPa)	ρ (kg m^{-3})	γ (mN m^{-1})	τ (ms)
PAAm 6.5%	0.16	1003.3	65.6	12.2 ± 1.6
PAAm 30.0%	366.6	1019.4	57.3	5.5 ± 0.3

addition, due to the intermediate elasticity values of the prepared PAAm, conventional shear rate ramp measurements performed for non-Newtonian liquids or compression tests performed for stiff solids cannot be used to characterize these materials.

For all the PAAm drops, the surface tension of each prepolymer solution was measured using the pendant drop technique on a drop-shape analyzer (DSA30, KRÜSS) under ambient conditions. To extract the surface tension, KRÜSS ADVANCE software's in-built Young-Laplace equation was used (see Table 1). Each measurement was repeated three times.

2.3 Imaging experiments

For static or equilibrium measurements, the PAAm drops/spheres were deposited on freshly cleaned glass substrates. Subsequently, side-view images were recorded under proper back-lit illumination using a camera (FASTCAM AX-200, Photron) coupled to a 4× objective lens and an adapter tube providing a spatial resolution of 4 μm per pixel. Static contact-angle measurements were performed using the sessile drop technique using a tangent fit in ImageJ.

For spreading experiments, the spherical drops were held at the tip of a hydrophobic PTFE-coated stainless steel needle and gently lowered to make contact with the substrates positioned underneath on a stage. The lowering speed of the needle was maintained at a few μm s^{-1} to ensure minimal vibration upon contact. As the drop made contact with the substrate, the growth of the drop–substrate footprint radius, *i.e.*, the spreading radius, was recorded using a high-speed camera (FASTCAM S12, Photron) at an acquisition rate of 50 000 frames per second. The camera was equipped with a 10× long working-distance objective lens providing a spatial resolution of 2 μm per pixel. Due to the field of view restrictions imposed by the high magnification lens and the camera frame rate, the entire drop–substrate footprint radius is not captured, and we tracked the growth of the spreading radius on one side, specifically the right contact line. This is particularly true for the PAAm with 6.5 wt% where the spreading radius is large. The experimental videography was analyzed using a custom-built edge detection scheme on Python, whereby the radial location of the moving contact line was detected in each frame over the entire duration of the spreading event. Furthermore, using the information of the radial location, the dynamic contact angle in each frame was measured using either a tangent fit or a first-order polynomial fit. Each measurement was repeated 3–5 times to ensure consistency.

3 Results and discussion

3.1 Static morphology

In Fig. 5, we show the static or equilibrium configurations of these PAAm spheres/drops with varying Young's modulus. For low monomer wt%, *i.e.*, low Young's modulus, the PAAm wets the glass substrates in a manner similar to Newtonian liquid drops such as water (Fig. 5, E_0 = 5.7 Pa). Note that the equilibrium contact angle θ_E is approximately 20° for this liquid-like PAAm. With increasing Young's modulus, they exhibit intermediate wetting/contact morphologies with decreasing contact radius and increasing contact angles. For very stiff PAAm (Fig. 5, E_0 = 366 kPa), the static configuration mimics that of a similarly sized glass sphere with $\theta_E \approx 164°$. From their equilibrium configurations, it is evident that, despite having similar surface tension values, they follow different trajectories upon initial deposition to arrive at different equilibrium contact radius/angle values. Consequently, we aim to resolve their spreading characteristics using our dynamic measurements. Note that the spreading of weakly elastic, polymeric liquid-like PAAm, *i.e.*, PAAm with 4 wt% monomer, was reported in our previous work.[33] Here, we focus on the spreading of PAAm having moderate and high Young's modulus values.

3.2 Spreading dynamics

In Fig. 6, we show the experimental snapshots of the early stages of contact of a moderately elastic PAAm (E_0 = 0.16 kPa) and a stiff PAAm (E_0 = 366 kPa) on glass substrates. It is evident that even when the Young's modulus is moderately high, the contact dynamics resemble spreading of liquids on partially wetting substrates, whereas for the stiffer PAAm, the dynamics remain in a JKR-type contact regime. Further, we observe that even though the dynamic contact angle for the moderately elastic PAAm gradually decreases during the course of spreading, for the stiffer one, it consistently remains high. Here, we will first elaborate on the dynamics of contact in terms of the dynamic spreading radius $r(t)$ and dynamic contact angle θ_D (Fig. 6). In Fig. 7, we show the evolution of the PAAm–substrate footprint radius, *i.e.*, the spreading radius r and the dynamic contact angle θ_D for PAAm 6.5 wt% (E_0 = 0.16 kPa) on glass. From the observed trajectory, the spreading behavior can be categorized into two distinct regimes separated approximately at t = 10 ms. For $t \leq 10$ ms, the growth of the spreading radius appears to obey a power-law behavior, $r \sim t^{\alpha}$, where the exponent α needs to be analyzed. For $t \geq 10$ ms, the spreading transitions to a different regime, which can be termed as arrested spreading or contact. This transition becomes more evident upon analyzing the evolution of the dynamic contact angle θ_D. For $t \leq 10$ ms, we observe a monotonic decrease in θ_D, whereas for $t \geq 10$ ms, we observe significant oscillations in θ_D. In the following sections, we will elaborate on these two distinct regimes observed.

3.2.1 Viscous-capillary spreading regime. Since we consider the initial regime to be analogous to the spreading of liquids, we treat the dynamics in the light of spreading laws

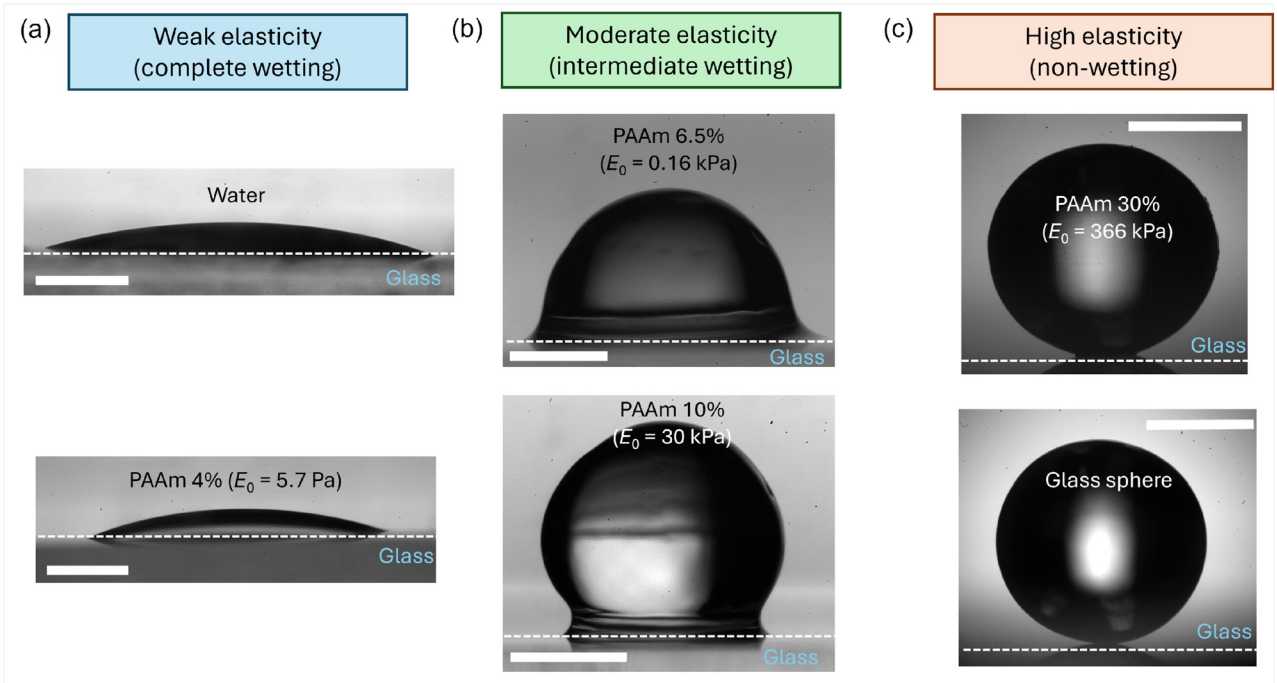

Fig. 5 Static configuration of (a) 1 mm radius water and PAAm with 4 wt% monomer drops on glass substrates, (b) 1 mm radius PAAm with 6.5 wt% monomer and PAAm with 10 wt% monomer drops on glass substrate, and (c) 1 mm radius PAAm with 30 wt% monomer spheres and glass beads on glass substrates. The elasticity E_0 values are shown. Scale bars represent 1 mm. Certain sub-figures are reproduced from authors' previous works with permission from the Royal Society of Chemistry[11] and the American Chemical Society, Copyright 2024.[15,33]

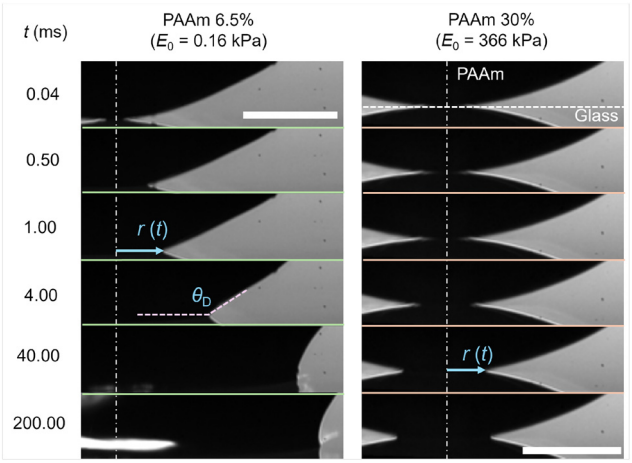

Fig. 6 High-speed imaging snapshots of the spreading of PAAm 6.5% drops (E_0 = 0.16 kPa, left column) and PAAm 30% spheres (E_0 = 366 kPa, right column) on glass substrates. $r(t)$ and θ_D are the spreading radius and dynamic contact angle, respectively. Scale bars represent 250 μm.

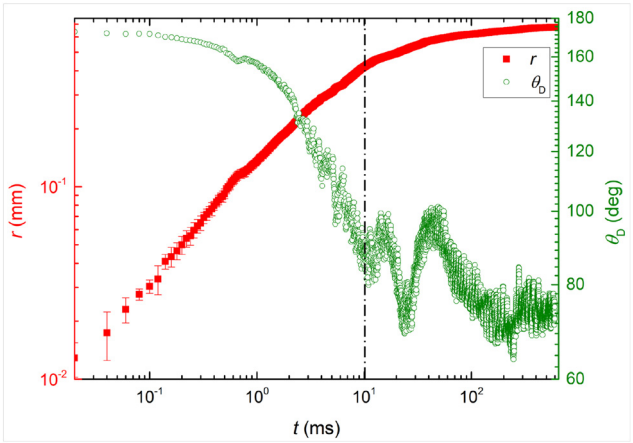

Fig. 7 Evolution of spreading radius r and dynamic contact angle θ_D for the spreading of 1 mm radius PAAm 6.5% drops (E_0 = 0.16 kPa) on glass substrates. The error bars in r represent the standard deviation of multiple experimental runs. The error bars in θ_D are omitted for clarity. The dashed line approximately demarcates regime I and regime II.

obeyed by liquids, either Newtonian or viscoelastic. From existing literature,[16–18,21] it is well understood that for the spreading of low-viscosity Newtonian liquids such as water, capillary-driven contact-line motion is resisted by liquid inertia, yielding the inertial-capillary scaling law for the spreading radius, $r \sim (\gamma R/\rho)^{1/4} t^{1/2}$ (see the SI for a detailed derivation). A similar power-law spreading is also observed for weakly elastic, shear-thinning liquids, *i.e.*, the viscous-capillary scaling law $r \sim (\gamma R/\mu)^{1/2} t^{1/2}$, where liquid viscosity is the dominant dissipation mechanism[33,42] (see the SI for a detailed derivation). Here, μ is the high-shear-rate viscosity, typically obtained from shear rate ramp measurements.[33] We compare both these power-law scalings with the observed spreading of the moderately elastic PAAm in regime I. However, although rheology measurements of high-shear-rate viscosity are straightforward

for weakly elastic, polymeric liquids, the same cannot be said for the PAAm 6.5%. With a Young's modulus of 0.16 kPa, *i.e.*, 3 orders of magnitude higher than conventional polymeric liquids, attempts to perform such measurements yielded anomalous flow curves and the samples often ruptured as well. Thus, we rely on our rheology fitting (Fig. 3) to extract the characteristic shear viscosity, *i.e.*, $\mu_0 = G_0\tau = 0.72$ Pa s. Note that since G_∞ is unrelaxed at high contact-line velocity (Fig. 4b), the system essentially behaves as a Maxwell fluid (μ, G_0) here. Furthermore, since the flow during regime I of the spreading is primarily extensional, we consider the extensional viscosity, $\mu = 6\mu_0 \approx 4$ Pa s.[43] Consequently, we use this value for comparison with the viscous capillary scaling law. Note that a Trouton ratio (μ/μ_0) of 6 is a reasonable assumption, although higher ratios are also observed, specifically during necking of viscoelastic filaments at high strain rates.[44,45]

In Fig. 8, we show the comparison of the observed spreading behavior in regime I with both the inertial-capillary and viscous-capillary scaling laws. For comparison, we also show the spreading of 1 mm radius DI water drops on glass substrates. From Fig. 8, it is evident that for moderately elastic PAAm, the spreading radius obey the scaling law $r \sim (\gamma R/\mu)^{1/2}t^{1/2}$, *i.e.*, a regime where liquid capillarity is resisted primarily by PAAm viscosity. Thus, the behavior is similar to the spreading of a viscous liquid (Newtonian or shear-thinning). It may seem counterintuitive that viscosity plays a dominant role in such an elastic system, especially when the contact-line velocity is relatively high. Consequently, we analyze the relaxation timescale of the material. For PAAm 6.5%, $\tau = 12$ ms, which is approximately the same as the spreading timescale in regime I, $t_0 \approx$ 10–20 ms, around which the transition to regime II is observed. Thus, the characteristic Deborah number during regime I of spreading is De = $\tau/t_0 \approx 0.6$–$1.2 \approx 1$, and hence the material response should ideally be viscoelastic rather than purely viscous. To interpret the observed discrepancy, we highlight that, phenomenologically, the polymer chains are unrelaxed in this regime. Thus, they can neither resist deformation nor store energy. From a constitutive model point of view, the high-frequency spring G_∞ is thus unrelaxed, and the system behaves as a Maxwell fluid where the viscous dashpot only contributes to the dissipation. At the same time, we note that for a purely viscous response to be effective, the spring with modulus G_0 should not contribute to any form of dissipation and can only store a small fraction of the capillary energy. Furthermore, note that the characteristic viscous-capillary timescale $t_v = \mu R/\gamma \approx 60$ ms $\approx 4t_0$, reinforcing our conclusions that this regime is viscous-dominated. Alternatively, one can also look at the characteristic Ohnesorge number of the system, $\mathrm{Oh} = \mu/\sqrt{\rho\gamma R} = 15.6 \gg 1$.

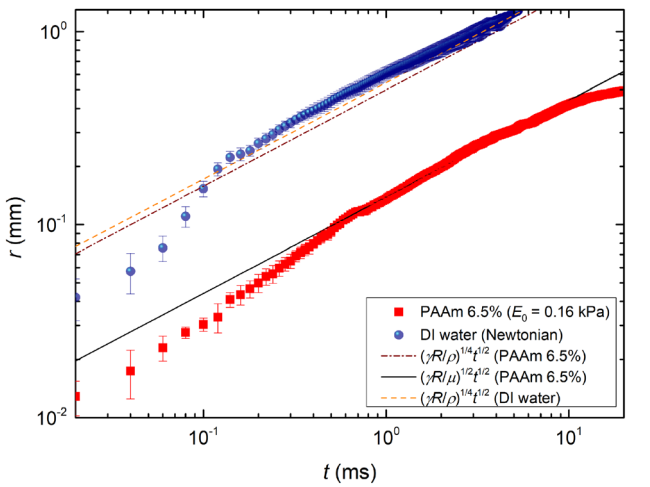

Fig. 8 Evolution of spreading radius r for 1 mm radius PAAm 6.5% (E_0 = 0.16 kPa) drops (red squares) and DI water drops (blue circles) on glass substrates. The different scaling laws are shown for clarity. The error bars represent the standard deviation of multiple experimental runs. Note that the deviation of our experimental data from the fitted scaling law aids us in identifying the duration of the initial regime.

3.2.2 Elasto-capillary regime. From Fig. 7, it is evident that the spreading transitions to regime II after $t \geq 10$ ms, where the rate of contact-line motion slows down significantly, accompanied by strong oscillations in the dynamic contact angle. To compare the different spreading rates, we highlight that the average contact-line velocity in regime I is $v_{CL} = \mathrm{d}r/\mathrm{d}t = 40$ mm s^{-1}, which subsequently drops to $v_{CL} = \mathrm{d}r/\mathrm{d}t = 0.33$ mm s^{-1} in regime II. The prominent decay in the spreading rate can be partly due to the decay in the capillary force driving the CL motion. However, since $t > \tau$ or conversely De < 1, the material response should ideally be in a transition phase. However, the observations of the oscillations in the dynamic contact angles indicate that a viscoelastic material response is dominant here. To elaborate on this, we recall that for fast capillary-inertial spreading of low-viscosity liquids such as water, contact angle oscillations are observed during regime I with a typical timescale $\delta t_{in} = \sqrt{\rho R^3/\gamma} \approx 4$ ms. Here, we do not observe such oscillations in regime I due to viscous damping, reinforcing our previous assertion of a purely viscous regime. However, in regime II, *i.e.*, for $t \geq 10$ ms, we observe oscillations with a typical duration of 500 ms. Additionally, the time periods of these oscillations are non-uniform and much greater than $\sqrt{\rho R^3/\gamma}$. We thus note that as polymers accumulate close to the moving contact line, they can be treated as a system of effective springs undergoing compression and relaxation, causing the observed oscillations in dynamic contact angles. Consequently, the high-frequency spring is relaxing and can resist deformation. Furthermore, G_∞ can assume any value between G_0 and βG_0. Phenomenologically, the polymer accumulation close to the contact line is manifested by a distinct foot-like region that retards motion. The foot-like region grows in size until equilibrium is reached. Furthermore, the onset of the foot-like region highlights that the spreading loses its extensional character and shear effects need to be accounted for.

To model the effect of elasticity and interpret the evolution of contact in this regime, we deviate from the conventional fluid mechanics approach. Thus, we first formulate the stress–strain relation relevant to this system: $\sigma = G_0 e + \mu_0(\mathrm{d}e/\mathrm{d}t')$, where $\sigma \sim \gamma R/r'^2$ is the Laplace pressure driving the contact line motion, and e is the strain. It is important to note that since

both the relaxed spring G_0 and the high-frequency spring G_∞, contribute in this regime, the effective viscosity of the dashpot can be expressed as $\mu_0 = (G_\infty - G_0)\tau = \beta(G_0 - 1)\tau \approx \beta G_0\tau$ since $\beta \gg 1$. Furthermore, note that, for the ease of analysis, we consider a variable change: $r' = r - r_0$ and $t' = t - t_0$, where r_0 and t_0 are the spreading radius and time at the end of regime I (see inset of Fig. 9). Thus, the strain can be expressed as $e \sim r'/r_0$. Consequently, the force balance per unit area of the CL can be expressed as

$$\frac{\gamma R}{r'^2} \sim G_0\frac{r'}{r_0} + \frac{\beta G_0\tau}{r_0}\left(\frac{\mathrm{d}r'}{\mathrm{d}t'}\right). \quad (1)$$

Eqn (1) is an approximate form of Bernoulli differential equation whose solution, with the initial condition $r' = 0$ at $t' = 0$, can be expressed as

$$r'(t') \sim \left(\frac{\gamma r_0 R}{\beta G_0}\right)^{1/3}\left[1 - \mathrm{e}^{-\frac{3t'}{\beta\tau}}\right]^{1/3}, \quad (2)$$

which can be expressed as

$$r(t) - r_0 \sim \left(\frac{\gamma r_0 R}{\beta G_0}\right)^{1/3}\left[1 - \mathrm{e}^{-\frac{3(t-t_0)}{\beta\tau}}\right]^{1/3}. \quad (3)$$

Note that in solving eqn (3), we use our experimentally observed r_0 and t_0 as inputs. In Fig. 9, we show the comparison of our theoretical model with experimental data. A reasonably good agreement is observed for $\beta = 50$. Note that this β value deviates from that obtained from our rheology fitting, *i.e.*, $\beta = 200$. Furthermore, we observe that using $\beta = 200$ to fit our experiments severely underestimates the data (see Fig. S3, SI). The discrepancy is likely due to the different dynamics involved in shear rheology and spreading. Furthermore, existing literature has typically used $\beta \sim 10$–100 to model dynamic contact-line problems,[46] and thus $\beta = 50$ is a reasonable assumption. Nevertheless, we highlight that our solution is extremely sensitive to β since it effectively prevents the exponential term in eqn (3) to go out of bounds. This also validates our assumption of using the standard linear model to represent the moving contact line, since for any other model, *e.g.*, Maxwell (μ, G_∞) or Kelvin–Voigt (μ, G_0), the β factor does not appear within the exponential term of the final solution. Furthermore, we point out that the spreading radius continues to grow slowly beyond what is shown in Fig. 7 and 9, until equilibrium is reached. However, due to the limited field of view at the chosen frame rate and magnification, the entire process cannot be captured.

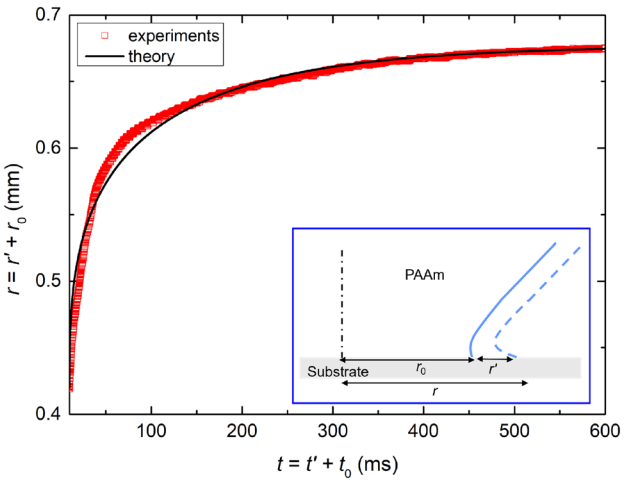

Fig. 9 Evolution of the spreading radius r for 1 mm radius PAAm 6.5% drops (E_0 = 0.16 kPa) on glass substrates in regime II. The symbols represent experimental data, whereas the solid line represents the theoretical solution (eqn (3)). Here, the origin of the x-axis is at t = 10 ms. The inset shows the schematic of the spreading process, highlighting the different variables r, r' and the radius at the end of regime I, r_0. Error bars are omitted for clarity.

3.3 Dynamics of spreading for highly elastic drops

For the much stiffer PAAm (E_0 = 366 kPa) sphere, we observe that the contact evolution is significantly slower with a much smaller final radius (Fig. 10). Qualitatively, the inherent characteristics remain the same: an initial regime obeying a power-law growth in the spreading radius, *i.e.*, $r \sim t^{1/2}$, and a final regime with an exponential decay with a transition point around 7–8 ms (Fig. 10a and b). In other words, t_0 = 7–8 ms, yielding the characteristic Deborah number of regime I, De = τ/t_0 = 1.2–1.4 $\approx$ 1. Thus, similar to the softer PAAm, these conditions also signify a transition to regime II. Furthermore, note that, in comparing our experimental data in regime II with our model (eqn (3)), a β value of 10 was used, which is on par with the value obtained from rheology. Compared to the spreading of moderately elastic PAAm with E_0 = 0.16 kPa, here the average contact-line velocity during regime I is $v_{CL} \approx 8$ mm s^{-1}, which decays to approximately 0.1 mm s^{-1} during regime II. Additionally, we observe that there are significant phenomenological differences between the two cases. Notably, we observe uniform oscillations of the spreading radius in regime II, which were previously not observed. Repeated measurements confirmed that these oscillations are not artificially induced by image processing and are an inherent part of the dynamics. Thus, despite reasonable agreement between our theoretical model (eqn (3)) and the experimental data (Fig. 10b), we highlight that our governing equation does not contain a second-order derivative term to accurately model such oscillations in r.[47]

Phenomenologically, the observed oscillations are likely due to the high elasticity of the PAAm, rendering significant resistance to the moving contact line. Note that, here also, the deformation foot exists in regime II of spreading. However, due to the large elasticity, the foot dimensions are very small and are only evident during higher-magnification imaging. Additionally, oscillations of the dynamic contact angle θ_D are also observed, which were previously observed during the spreading of moderately elastic PAAm as well (Fig. 10c). However, compared to the oscillations observed for the spreading of PAAm 6.5 wt%, here we observe that the oscillations are more uniform. Both the oscillations in dynamic contact radius and dynamic contact angle have a uniform time period $\delta t \approx$ 30 ms (Fig. 10b and c). Considering capillarity and elasticity

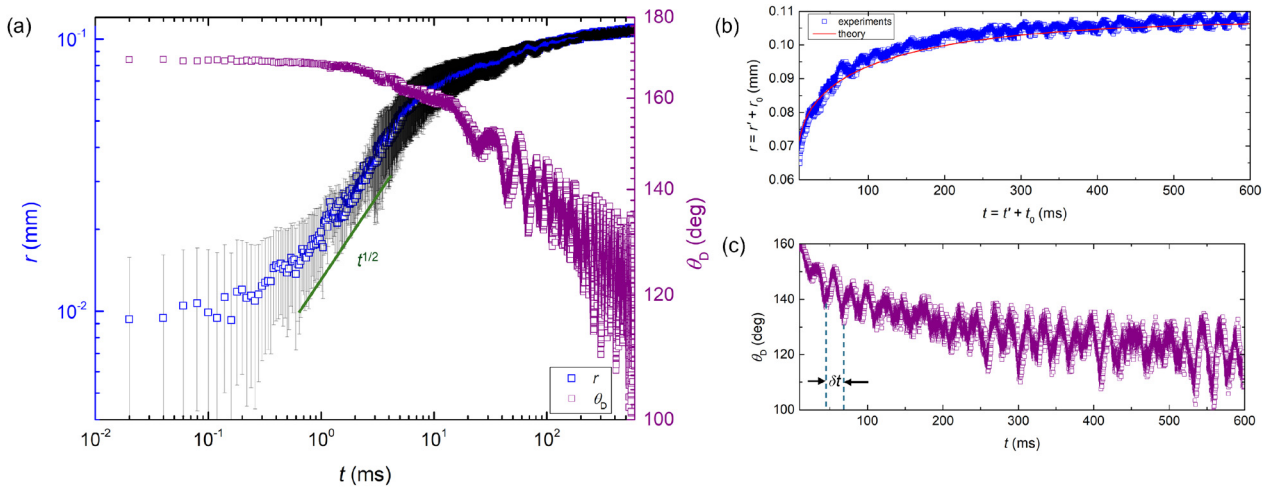

Fig. 10 (a) Evolution of spreading radius r and dynamic contact angle θ_D for 1 mm radius PAAm 30% drops (E_0 = 366 kPa) on glass substrates. The $r \sim t^{1/2}$ scaling law is shown for clarity. The error bars represent the standard deviation of multiple experimental runs. (b) Evolution of spreading radius r in regime II. The symbols represent experimental data, whereas the solid line represents the theoretical solution (eqn (3)). Here, the origin of the x-axis is at t = 7.5 ms. Error bars are omitted for clarity. (c) Evolution of the dynamic contact angle θ_D in regime II. δt represents the time period of oscillations. Here, the origin of the x-axis is at t = 7.5 ms.

effects, the characteristic timescale of oscillations can be expressed as $\gamma/G_0 v_{CL} \approx 60$ ms, which is in reasonable agreement with our experimental data. Finally, we highlight that the significant error bars in Fig. 10a are due to the use of side-view imaging and a small contact radius involved at the early moments of contact. This can be circumvented by the use of bottom-view imaging.[18,20]

Combining eqn (3) with our experimental results has interesting implications. As $t \to \infty$ and $\beta \to 1$, $r \to (\gamma r_0 R/G_0)^{1/3} + r_0$. This limit can provide us with predictions of the equilibrium contact radius. For the spreading of PAAm 6.5 wt% (E_0 = 0.16 kPa), $r_0 \approx 0.4R$ (Fig. 7) and thus $r \to 0.7(\gamma R^2/G_0)^{1/3} + 0.4R$. However, for the spreading of PAAm 30 wt% (E_0 = 366 kPa), $r_0 \approx 0.06R$ (Fig. 10) and thus the second term can be neglected. Consequently, we have $r \to 0.4(\gamma R^2/G_0)^{1/3} \sim (\gamma R^2/G_0)^{1/3}$, *i.e.*, it recovers the JKR theory[4] at equilibrium. Note that the small deviation from the JKR theory for the moderately elastic PAAm is reasonable since the strain involved at equilibrium is beyond the Hookean limit. Finally, we briefly comment on any possible dehydration of the polymer network, which can affect our experimental findings. Note that the PAAm spheres contain significant quantities of water. However, the characteristic diffusion coefficient, $D \sim 10^{-9}$ m s^{-1}, renders the diffusion timescale to be around 1000 s.[13] Since the characteristic timescale of early regimes of spreading is around 1 s, dehydration of the PAAm does not interfere with our experimental observations.

Here, we highlight the significance of these findings for 3D printing applications.[34,48,49] In particular, during the deposition of the initial layer, the viscoelastic properties of the ink or resin are critical. Traditional materials research tends to emphasize ink rheology,[50] with oscillatory shear rheology being a common tool. However, this method does not accurately replicate the dynamic conditions of 3D printing. Extensional rheology techniques, such as Capillary Breakup Extensional Rheology (CaBER), also have limitations, notably the absence of moving contact lines.[51,52] Dynamic wetting studies, by contrast, offer a promising approach to simulate the interplay between viscoelasticity and contact-line motion.[33,41,53] Notably, most commercial 3D printers, such as the Formlabs Form 4 and Uniz Slash Plus UDP, operate at speeds ranging from 0.01 to 100 mm s^{-1}, which aligns well with our experimental conditions.[54,55] Since both material viscoelasticity and printing speed jointly influence final print resolution, our work provides valuable insights for optimizing these parameters to achieve high-resolution prints.

4 Conclusions

In conclusion, using experiments and theory, we show the short-time spreading behavior of (visco)elastic drops across a wide range of Young's modulus, where both liquid-like wetting and solid-bead-like contact configurations are possible. For moderate to high Young's modulus values, we observe that the short-time spreading behavior is distinctly different from that observed for Newtonian liquid drops, such as water, or non-Newtonian, shear-thinning liquids, such as PEO and Carbopol. In particular, the dynamics exhibit two distinct regimes: an early viscous regime followed by a viscoelastic regime, with a crossover time dictated by the condition De $\approx$ 1. While the former shows a power-law evolution in the spreading radius, the latter exhibits an exponential decay. We interpret the former regime as a competition between the relevant capillary and viscous forces. The latter regime is interpreted using the standard linear model of viscoelasticity. Furthermore, our theoretical formulation leads to the JKR theory in the equilibrium limit and can, in principle, be used to construct a dynamic JKR theory. Additionally, we highlight how the rheology of the polymers validates our assumption of the standard

linear model of viscoelasticity. Specifically, we observe that this model is better suited to explain dynamical polymeric systems like the present ones, compared to other constitutive models such as Kelvin–Voigt, Maxwell, Oldroyd-B, or Saramito. A similar model was used by de Gennes to describe the dynamics of crack propagation in soft adhesives, also referred to as de Gennes' trumpet model.[37]

The findings presented here can be used to understand cell spreading, which involves similar elastic properties.[56] Furthermore, they can provide a guiding principle for material selection in 3D printing using hydrogels and biomaterial inks,[57,58] where viscoelasticity plays a key role in indicating the final achievable print resolution. Combined with the non-trivial contact velocity at which such printing processes typically operate, the present short-time spreading study offers routes to control print speeds for viscoelastic inks.

Author contributions

S. K. M. conceived the study. S. M. and A.-R. K. performed the experiments and analyzed the data. All authors discussed the results. S. M. wrote the manuscript with input from all the authors. B. Z. and S. K. M. supervised the research.

Conflicts of interest

The authors declare no conflict of interest.

Data availability

All data that support the findings of this study are included within the article.

The data supporting this article have been included as part of the supplementary information (SI). Supplementary information is available. See DOI: https://doi.org/10.1039/d5ma00896d.

Acknowledgements

The authors are grateful to Lukas Bauman (Department of Chemical Engineering, University of Waterloo) for assistance with PAAm preparation and Prof. Michael K. C. Tam (Department of Chemical Engineering, University of Waterloo) for providing the dynamic shear rheometer. B. Z. acknowledges the support of NSERC RGPIN-2019-04650. S. K. M. acknowledges the support of the Discovery Grant (NSERC, RGPIN-2024-03729).

References

1 P.-G. de Gennes, *Rev. Mod. Phys.*, 1985, **57**, 827.
2 D. Bonn, J. Eggers, J. Indekeu, J. Meunier and E. Rolley, *Rev. Mod. Phys.*, 2009, **81**, 739.
3 H. Hertz, *J. für die reine Angew. Math.*, 1882, **92**, 22.
4 K. L. Johnson, K. Kendall and A. D. Roberts, *Proc. R. Soc. London, Ser. A*, 1971, **324**, 301–313.
5 T. Young, *Philos. Trans. R. Soc. London*, 1805, 65–87.
6 E. R. Jerison, Y. Xu, L. A. Wilen and E. R. Dufresne, *Phys. Rev. Lett.*, 2011, **106**, 186103.
7 A. Marchand, S. Das, J. H. Snoeijer and B. Andreotti, *Phys. Rev. Lett.*, 2012, **109**, 236101.
8 S. J. Park, B. M. Weon, J. S. Lee, J. Lee, J. Kim and J. H. Je, *Nat. Commun.*, 2014, **5**, 4369.
9 S. Mitra, S. Misra, T. Tran and S. K. Mitra, *Langmuir*, 2022, **38**, 7750–7758.
10 R. W. Style, C. Hyland, R. Boltyanskiy, J. S. Wettlaufer and E. R. Dufresne, *Nat. Commun.*, 2013, **4**, 2728.
11 A.-R. Kim, S. Mitra, S. Shyam, B. Zhao and S. K. Mitra, *Soft Matter*, 2024, **20**, 5516–5526.
12 A. Chakrabarti, A. Porat, E. Raphaël, T. Salez and M. K. Chaudhury, *Langmuir*, 2018, **34**, 3894–3900.
13 J. Yang, R. Bai, B. Chen and Z. Suo, *Adv. Funct. Mater.*, 2020, **30**, 1901693.
14 W. Zhang, R. Wang, Z. Sun, X. Zhu, Q. Zhao, T. Zhang, A. Cholewinski, F. K. Yang, B. Zhao and R. Pinnaratip, *et al.*, *Chem. Soc. Rev.*, 2020, **49**, 433–464.
15 P. Chakraborty, S. Mitra, A.-R. Kim, B. Zhao and S. K. Mitra, *Langmuir*, 2024, **40**, 7168–7177.
16 A.-L. Biance, C. Clanet and D. Quéré, *Phys. Rev. E: Stat., Nonlinear, Soft Matter Phys.*, 2004, **69**, 016301.
17 J. C. Bird, S. Mandre and H. A. Stone, *Phys. Rev. Lett.*, 2008, **100**, 234501.
18 S. Mitra and S. K. Mitra, *Langmuir*, 2016, **32**, 8843–8848.
19 Q. Vo, S. Mitra, M. Lin and T. Tran, *J. Colloid Interface Sci.*, 2024, **664**, 478–486.
20 A. Eddi, K. G. Winkels and J. H. Snoeijer, *Phys. Fluids*, 2013, **25**, 013102.
21 K. G. Winkels, J. H. Weijs, A. Eddi and J. H. Snoeijer, *Phys. Rev. E: Stat., Nonlinear, Soft Matter Phys.*, 2012, **85**, 055301.
22 A. Carlson, G. Bellani and G. Amberg, *Phys. Rev. E: Stat., Nonlinear, Soft Matter Phys.*, 2012, **85**, 045302.
23 J. D. Paulsen, J. C. Burton and S. R. Nagel, *Phys. Rev. Lett.*, 2011, **106**, 114501.
24 D. Debnath, P. Kumar and S. K. Mitra, *Langmuir*, 2021, **37**, 14833–14845.
25 R. Cox, *J. Fluid Mech.*, 1986, **168**, 169–194.
26 L. Tanner, *J. Phys. D: Appl. Phys.*, 1979, **12**, 1473.
27 S. Chen, E. Pirhadi and X. Yong, *J. Colloid Interface Sci.*, 2022, **618**, 283–289.
28 D. Cuvelier, M. Théry, Y.-S. Chu, S. Dufour, J.-P. Thiéry, M. Bornens, P. Nassoy and L. Mahadevan, *Curr. Bio.*, 2007, **17**, 694–699.
29 A. Bouillant, P. J. Dekker, M. A. Hack and J. H. Snoeijer, *Phys. Rev. Fluids*, 2022, **7**, 123604.
30 S. Yada, K. Bazesefidpar, O. Tammisola, G. Amberg and S. Bagheri, *Phys. Rev. Fluids*, 2023, **8**, 043302.
31 S. C. Varma, A. Saha, S. Mukherjee, A. Bandopadhyay, A. Kumar and S. Chakraborty, *Soft Matter*, 2020, **16**, 10921–10927.
32 S. C. Varma, D. Dasgupta and A. Kumar, *Phys. Fluids*, 2022, **34**, 093112.
33 S. Mitra, A.-R. Kim, B. Zhao and S. K. Mitra, *Langmuir*, 2024, **40**, 18968–18976.

34 J. M. Townsend, E. C. Beck, S. H. Gehrke, C. J. Berkland and M. S. Detamore, *Prog. Polym. Sci.*, 2019, **91**, 126–140.
35 S. Mitra, A.-R. Kim, B. Zhao and S. K. Mitra, *Soft Matter*, 2025, **21**, 4587–4595.
36 I. M. Ward and J. Sweeney, *Mechanical properties of solid polymers*, John Wiley & Sons, 2012.
37 P.-G. de Gennes, *Langmuir*, 1996, **12**, 4497–4500.
38 Y. M. Efremov, T. Okajima and A. Raman, *Soft Matter*, 2020, **16**, 64–81.
39 J. Hinch and O. Harlen, *J. Non-Newtonian Fluid Mech.*, 2021, **298**, 104668.
40 P. Saramito, *J. Non-Newtonian Fluid Mech.*, 2007, **145**, 1–14.
41 H. L. França, M. Jalaal and C. M. Oishi, *Phys. Rev. Res.*, 2024, **6**, 013226.
42 S. Das, P. R. Waghmare and S. K. Mitra, *Phys. Rev. E: Stat., Nonlinear, Soft Matter Phys.*, 2012, **86**, 067301.
43 T. Sridhar, V. Tirtaatmadja, D. Nguyen and R. Gupta, *J. Non-Newtonian Fluid Mech.*, 1991, **40**, 271–280.
44 S. L. Anna and G. H. McKinley, *J. Rheol.*, 2001, **45**, 115–138.
45 A. Chowdhury, S. Misra, S. Mitra and S. K. Mitra, *Langmuir*, 2025, **41**, 11358–11366.
46 S. Karpitschka, S. Das, M. van Gorcum, H. Perrin, B. Andreotti and J. H. Snoeijer, *Nat. Commun.*, 2015, **6**, 7891.
47 C.-A. Charles, A. Louhichi, L. Ramos and C. Ligoure, *Soft Matter*, 2021, **17**, 5829–5837.
48 R. C. Daniel and J. C. Berg, *Adv. Colloid Interface Sci.*, 2006, **123**, 439–469.
49 M. T. Arango, Y. Zhang, C. Zhao, R. Li, G. Doerk, D. Nykypanchuk, Y. K. Chen-Wiegart, A. Fluerasu and L. Wiegart, *Mater. Today Phys.*, 2020, **14**, 100220.
50 A. Corker, H. C.-H. Ng, R. J. Poole and E. Garca-Tuñón, *Soft Matter*, 2019, **15**, 1444–1456.
51 M. Rosello, S. Sur, B. Barbet and J. P. Rothstein, *J. Non-Newtonian Fluid Mech.*, 2019, **266**, 160–170.
52 O. Arnolds, H. Buggisch, D. Sachsenheimer and N. Willenbacher, *Rheol. Acta*, 2010, **49**, 1207–1217.
53 J. van der Kolk, D. Tieman and M. Jalaal, *J. Fluid Mech.*, 2023, **958**, A34.
54 https://www.uniz.com/eu_en/3d-printers/slash-2.
55 https://formlabs.com/3d-printers/professional.
56 U. S. Schwarz and S. A. Safran, *Rev. Mod. Phys.*, 2013, **85**, 1327.
57 L. Bauman and B. Zhao, *J. Colloid Interface Sci.*, 2023, **638**, 882–892.
58 J. Li, C. Wu, P. K. Chu and M. Gelinsky, *Mater. Sci. Eng., R*, 2020, **140**, 100543.